



PAPER

An ytterbium quantum gas microscope with narrow-line laser cooling

OPEN ACCESS

RECEIVED

10 September 2015

REVISED

21 December 2015

ACCEPTED FOR PUBLICATION

7 January 2016

PUBLISHED

1 February 2016

Original content from this work may be used under the terms of the [Creative Commons Attribution 3.0 licence](https://creativecommons.org/licenses/by/4.0/).

Any further distribution of this work must maintain attribution to the author(s) and the title of the work, journal citation and DOI.



Ryuta Yamamoto, Jun Kobayashi, Takuma Kuno, Kohei Kato and Yoshiro Takahashi

Department of Physics, Graduate School of Science, Kyoto University, Japan 606–8502

E-mail: r_yamamoto@scphys.kyoto-u.ac.jp

Keywords: cold atoms, optical lattice, laser cooling, quantum gas microscope

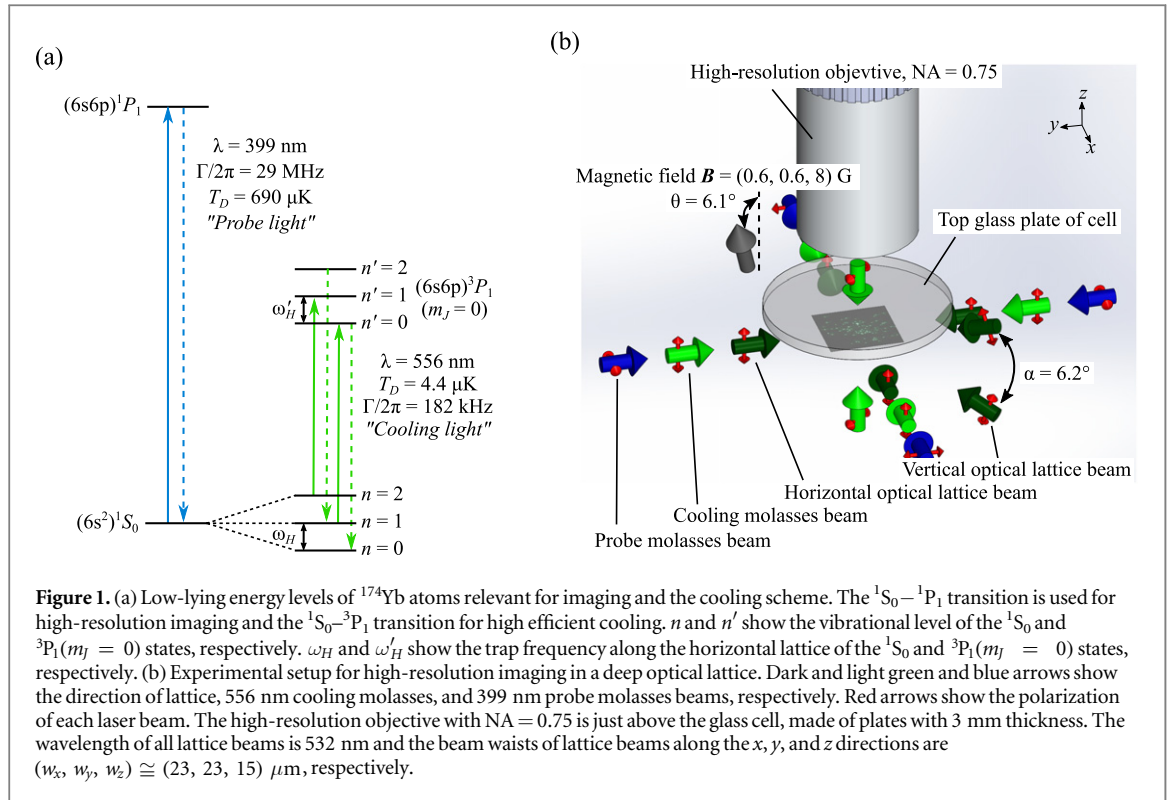
Abstract

We demonstrate site-resolved imaging of individual bosonic ^{174}Yb atoms in a Hubbard-regime two-dimensional optical lattice with a short lattice constant of 266 nm. To suppress the heating by probe light with the $^1\text{S}_0$ – $^1\text{P}_1$ transition of the wavelength $\lambda = 399$ nm for high-resolution imaging and preserve atoms at the same lattice sites during the fluorescence imaging, we simultaneously cool atoms by additionally applying narrow-line optical molasses with the $^1\text{S}_0$ – $^3\text{P}_1$ transition of the wavelength $\lambda = 556$ nm. We achieve a low temperature of $T = 7.4(13)$ μK , corresponding to a mean oscillation quantum number along the horizontal axes of 0.22(4) during the imaging process. We detect, on average, 200 fluorescence photons from a single atom within a 400 ms exposure time, and estimate a detection fidelity of 87(2)%. The realization of a quantum gas microscope with enough fidelity for Yb atoms in a Hubbard-regime optical lattice opens up the possibilities for studying various kinds of quantum many-body systems such as Bose and Fermi gases, and their mixtures, and also long-range-interacting systems such as Rydberg states.

1. Introduction

Ultracold quantum gases in optical lattices have proven extremely useful for the study of quantum phases and the dynamical evolutions of strongly correlated many-body system described by a Hubbard model [1]. Well-known examples include a quantum phase transition from a superfluid (SF) to a Mott insulator (MI) for bosonic species [2–4], and a crossover from a metal to a MI for fermionic species [5, 6]. To fully exploit the potential of ultracold atoms in an optical lattice as a quantum simulator, it is a great advantage to have access to the in-trap atom distribution with single-atom resolution. In 2009, a quantum gas microscope (QGM) was realized with bosonic ^{87}Rb for the first time [7]. Site-resolved imaging has been used to study the SF to MI transition [8, 9], and strongly correlated dynamics in optical lattices [10–12]. Site-resolved imaging systems have been realized for other alkaline atomic species such as fermionic ^{40}K [13–15] and ^6Li [16–18] very recently.

Extending the applicability of a QGM technique to atomic species beyond alkali-metal atoms is an important step for a further revolution. In particular, a successful application of a QGM technique to two-electron atoms such as alkaline-earth metal and ytterbium (Yb) atoms is remarkable because it offers many unique possibilities for quantum simulation and quantum information research. In fact, recent studies demonstrate that a system of two-electron atoms in an optical lattice is an ideal platform for the study of $\text{SU}(\mathcal{N})$ physics [19–22], two-orbital $\text{SU}(\mathcal{N})$ physics [23–26], and topological physics [27]. In addition, a variety of stable isotopes, 5 bosonic and 2 fermionic isotopes in the case of Yb atoms for example, enable us to study various kinds of many-body systems such as ultracold Bose and Fermi gases and Bose–Bose [28, 29], Bose–Fermi [29–31], and Fermi–Fermi [20] mixtures in an optical lattice. The existence of nuclear spin degrees of freedom in the ground state $^1\text{S}_0$ and long-lived metastable states $^3\text{P}_0$ and $^3\text{P}_2$ offers unique possibilities for quantum memory and quantum computation [32–35]. Additionally we can tune interatomic interactions between the $^1\text{S}_0$ and $^3\text{P}_2$ states by an anisotropy-induced magnetic Feshbach resonance [36]. Furthermore, a high-resolution laser spectroscopy of atoms in an optical lattice using the ultranarrow $^1\text{S}_0$ – $^3\text{P}_0$ and $^1\text{S}_0$ – $^3\text{P}_2$ optical transitions is also demonstrated both for bosons and fermions, revealing the novel behaviour of the atomic interaction of the system [24–26, 36, 37]. There has been also considerable interest in high-lying Rydberg states of two-electron atoms [38, 39] in an optical lattice

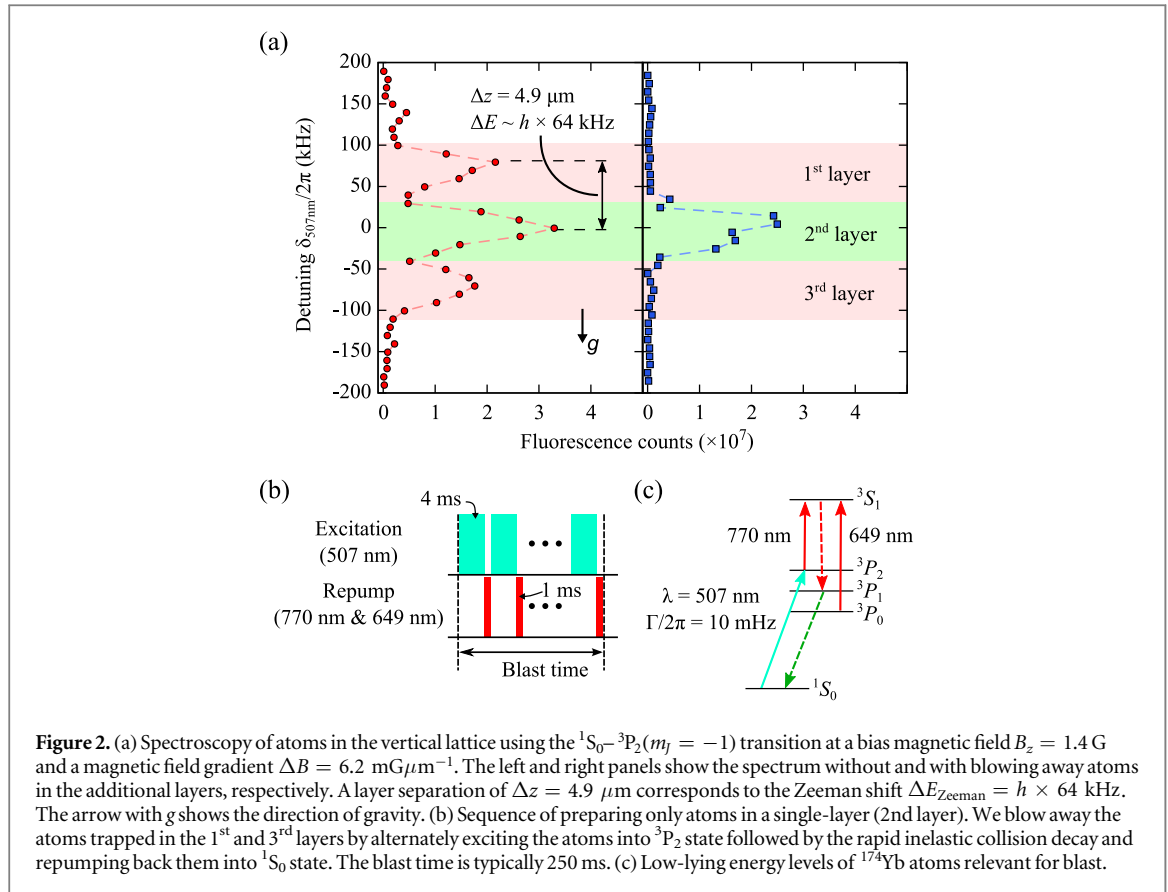


[40] because of an additional degrees of freedom for probing and manipulation provided by the remaining valence electron of a singly excited Rydberg state. The successful application of a QGM technique to these systems will definitely enhance our understanding of the physics described in the above.

The important progress towards this direction has been reported quite recently in [41], in which a site-resolved imaging system has been realized without cooling process for ^{174}Yb atoms in a two-dimensional (2D) optical lattice with a lattice constant of 544 nm. The achieved resolution of ~ 310 nm (full width at half maximum, FWHM) is impressively small. A further study is still necessary, however, to successfully perform the above mentioned interesting researches for Yb atoms using a QGM. First, a crucial aspect of QGM is the high-fidelity of the imaging process characterized by loss and hopping rates during the fluorescence imaging, which should be evaluated by comparing two successive images taken for the same atoms. Second, the Hubbard-regime optical lattice needs a shorter lattice constant, especially for heavier atoms of Yb. These conditions should be simultaneously satisfied with the single-site resolved imaging and single-atom sensitivity.

In this work, we achieve site-resolved imaging of individual ^{174}Yb atoms in a 2D optical lattice with a short lattice constant of 266 nm which ensures the Hubbard-regime [42]. To keep atoms at the same lattice sites during the fluorescence imaging, we simultaneously cool atoms by additionally applying narrow-line optical molasses with the $^1S_0 - ^3P_1$ transition ($\lambda = 556$ nm, the Doppler limit temperature $T_D = 4.4$ μK , natural linewidth $\Gamma/2\pi = 182$ kHz), resulting in a low temperature of $T = 7.4(13)$ μK , corresponding to a mean oscillation quantum number along the horizontal axes 0.22(4) during imaging process (see figure 1(a) for relevant energy levels). In particular, the careful tuning of the relative angle between an applied magnetic field and a polarization of lattice laser beams realizes the cancellation of the inhomogeneity of the light-shifts, which enhances a cooling efficiency of narrow-line laser cooling, both for sideband cooling along the horizontal direction and Doppler cooling along the vertical direction. The realization of such high efficient cooling allows for the suppression of heating due to the probe light using the $^1S_0 - ^1P_1$ transition ($\lambda = 399$ nm, the Doppler limit temperature $T_D = 690$ μK , natural linewidth $\Gamma/2\pi = 29$ MHz) for high-resolution imaging (see figure 1(a)). We achieve a lifetime $\tau > 7$ s of atoms during fluorescence imaging much longer than a typical imaging time of 400 ms, enabling to take multiple images for the same atomic sample and to successfully estimate the imaging fidelity to be 87(2)%. The realization of a QGM with enough fidelity for Yb atoms in a Hubbard-regime optical lattice opens up the possibilities for studying various kinds of quantum many-body systems such as Bose and Fermi gases, and their mixtures in an optical lattice, and also long-range-interacting systems such as Rydberg states.

The paper is organized as follow. In section 2, we describe an experimental setup and a method for preparation of an atom sample in a 2D lattice system. Section 3 presents cooling mechanism for realization of a



site-resolved imaging and section 4 shows the results of the analysis of site-resolved fluorescence images including loss and hopping rates. Finally we conclude our work with brief prospects in section 5.

2. Experimental setup and atom preparation

Our experiment starts from loading ^{174}Yb atoms into a magneto-optical trap (MOT) in a metal chamber and transferring the atoms into a glass cell (Schott AG BOROFLOAT) using an optical tweezer (OT). The detail of the MOT and OT setup is described in [43]. The position of atoms in the glass cell is about 5.5 mm below the surface of the glass cell, and just 6.23 mm under a high-resolution objective with numerical aperture of $\text{NA} = 0.75$ (Mitutoyo G Plan Apo HR50x (custom)), which is schematically shown in figure 1(b). After creating a Bose–Einstein condensate (BEC) of 5×10^4 atoms after 10 s evaporative cooling in a crossed optical trap formed by the OT beam and another 532 nm beam, we load the BEC into a vertical lattice generated by the interference of two laser beams with the wavelength of $\lambda = 532$ nm propagating at a relative angle of $\alpha = 6.2^\circ$. The vertical lattice has a spacing of $\lambda/(2 \sin(\alpha/2)) = 4.9$ μm and the trap frequency along the vertical axis (z -axis) of $\omega_z = 2\pi \times 2$ kHz at this loading stage, as explained in detail in our previous work [44].

The atoms, just after being loaded into the vertical lattice, spread over several, typically three, layers, as shown in the left panel of figure 2(a). In this situation, although we can focus on the atoms in one selected layer with an objective depth of less than 1 μm , we always have contributions from the atoms in other layers which considerably blur the image. To observe a clear image of the atoms in only one layer, we blow away the atoms in unnecessary layers. This is done by alternately exciting the atoms into the $^3P_2(m_J = -1)$ state under a bias magnetic field $B = 1.4$ G and a magnetic field gradient $\Delta B = 6.2$ mG μm^{-1} , corresponding to the Zeeman shift $\Delta E_{\text{Zeeman}} = h \times 64$ kHz/layer, followed by the rapid inelastic collisional decay and repumping back the atoms into the ground state (see figure 2(b)). Here the ultranarrow optical transition of $^1S_0 - ^3P_2(m_J = -1)$ with the resonant wavelength of 507 nm and natural linewidth $\Gamma/2\pi = 10$ mHz is used for the excitation and $^3P_2(m_J = -1) - ^3S_1$ and $^3P_0 - ^3S_1$ for repumping (see figure 2(c)). As a result, we successfully prepare the atoms in only a single layer, as shown in the right panel of figure 2(a).

Finally, we load the 2D atom cloud in a single layer into horizontal 2D optical lattices (x - and y -axes) by simultaneously ramping up the potential of the vertical and horizontal optical lattices, where the wavelength of horizontal lattices is $\lambda = 532$ nm and the lattice spacing is 266 nm. The vibrational frequencies along the three

axes at the fluorescence imaging stage are $(\omega_x, \omega_y, \omega_z) = 2\pi \times (300, 300, 15.7)$ kHz, corresponding to the lattice depths of $(U_x, U_y, U_z) = k_B \times (300, 300, 250)$ μ K, respectively.

3. Narrow-line laser cooling in an optical lattice

An important prerequisite for realizing a QGM is to preserve the atoms at their sites during fluorescence imaging. The $^1S_0 - ^1P_1$ transition provides high-resolution imaging with the diffraction limited resolution of a FWHM of 274 nm in our system. However, the high Doppler cooling limit temperature $T_D = 690$ μ K makes quite difficult to preserve atoms at their sites. In addition, the lack of hyperfine structure in the ground state 1S_0 of bosonic Yb atom makes impossible to apply sub-Doppler cooling techniques such as polarization-gradient cooling and Raman sideband cooling. To resolve this difficulty, we simultaneously cool the atoms with Doppler and sideband cooling using the $^1S_0 - ^3P_1$ narrow-line transition.

To efficiently cool all the atoms in an optical lattice with the narrow-line transition $^1S_0 - ^3P_1$, we need to suppress the inhomogeneity of light shift between the 1S_0 and 3P_1 states, otherwise the detuning for cooling is not optimized simultaneously for all atoms. Here the light shift in the ground state 1S_0 is given by $\Delta E_g^L = -(1/4)\alpha_g I$, where I is the laser intensity of the wavelength $\lambda = 532$ nm and $\alpha_g = 37.9$ Hz/(Wcm⁻²) is the calculated scalar polarizability in the 1S_0 state. The light shift in the magnetic sublevel m_j of the 3P_1 state is given as [45]

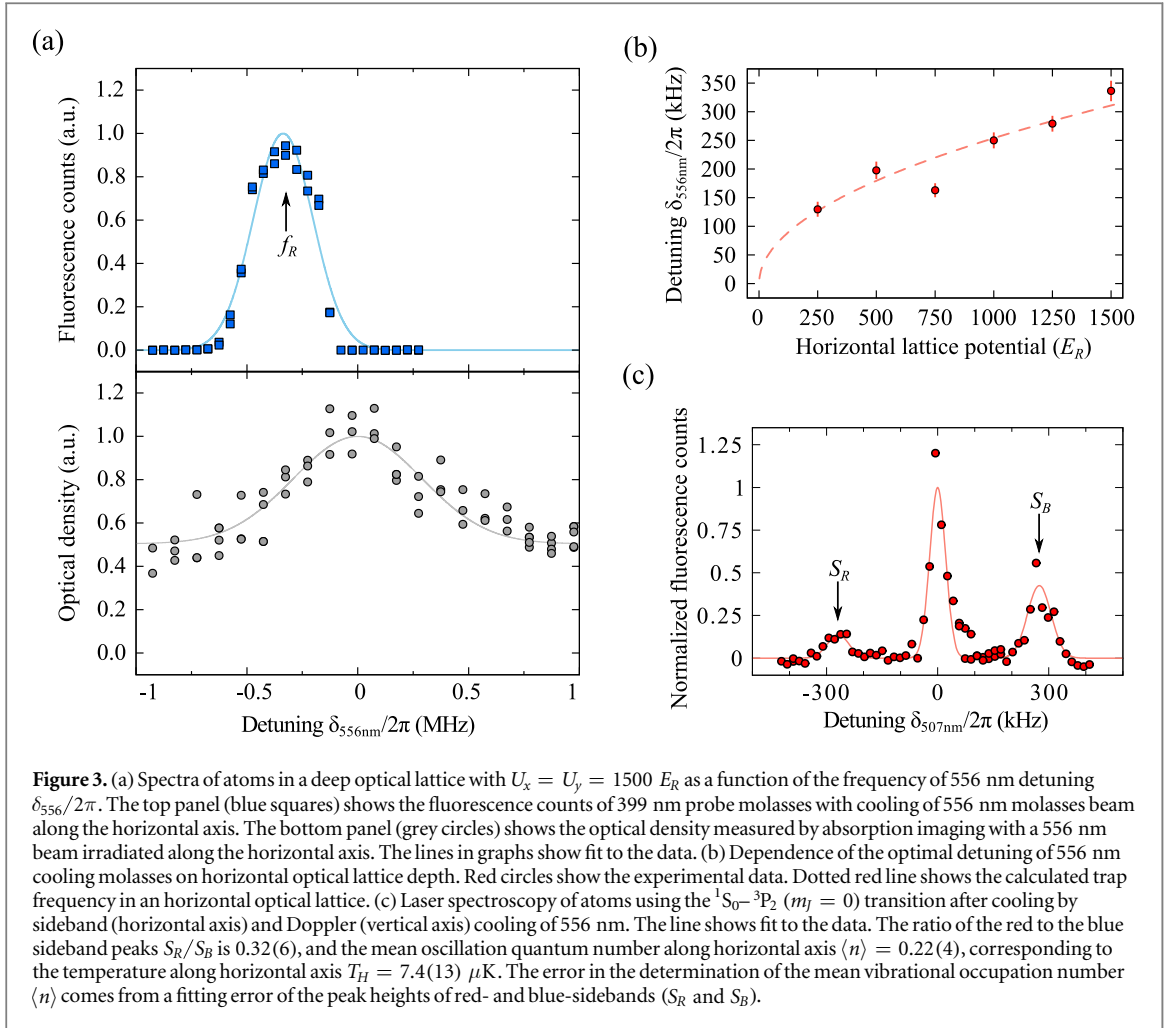
$$\Delta E_e^L = -\frac{1}{4}\alpha_e(m_j, \theta) I, \quad (1)$$

where

$$\alpha_e(m_j, \theta) = \alpha_e^S - \alpha_e^T \frac{1 - 3\cos^2\theta}{2} (3m_j^2 - 2). \quad (2)$$

Here θ is the angle between the quantization axis and the polarization of laser beams, α_e^S and α_e^T are the scalar and tensor polarizabilities in the 3P_1 state, respectively. Importantly, equation (2) provides the possibility of tuning the polarizability $\alpha_e(m_j, \theta)$ to coincide with α_g by choosing an appropriate angle θ for m_j , thus canceling the light-shift effects of the $^1S_0 - ^3P_1$ transition. For this possibility we perform a laser spectroscopy with the $^1S_0 - ^3P_1$ transition for various laser intensities and angles θ , and accurately determine α_e^S and α_e^T as 22.4(2) and $-7.6(1)$ Hz/(Wcm⁻²), respectively. With these values, our current setup of the polarizations of all the lattice beams parallel to the vertical axis provides $\alpha_e(m_j = 0, \theta = 0)/\alpha_g = 0.99$. In our experiment, however, we slightly tilt a magnetic field from the vertical direction by an angle 6.1° which gives $\alpha_e(m_j = 0, \theta = 6.1^\circ)/\alpha_g = 0.98$. This setup enables us to excite the atoms into the $^3P_1(m_j = 0)$ state, when the polarizations of the 556 nm cooling light along the horizontal axes are set to vertical, and those along the vertical axis horizontal (see figure 1(b)). Note that the light shift of the $^1S_0 - ^3P_1$ transition for probing is smaller than the natural linewidth of this transition of 29 MHz, and so it is not a problem. The total intensities of 399 nm and 556 nm beams correspond to the saturation parameters of $s_{399} \sim 1 \times 10^{-3}$ and $s_{556} \sim 1$, respectively. With this dual molasses, Moiré patterns of about 6 μ m pitch are observed as a result of the interference between the cooling molasses beam of 556 nm and the optical lattice of 532 nm. To erase this unwanted Moiré pattern, we modulate the phase of the standing wave of the 556 nm optical molasses by modulating retro-reflecting mirrors via the attached Piezo transducers, as explained in detail in our previous work [44].

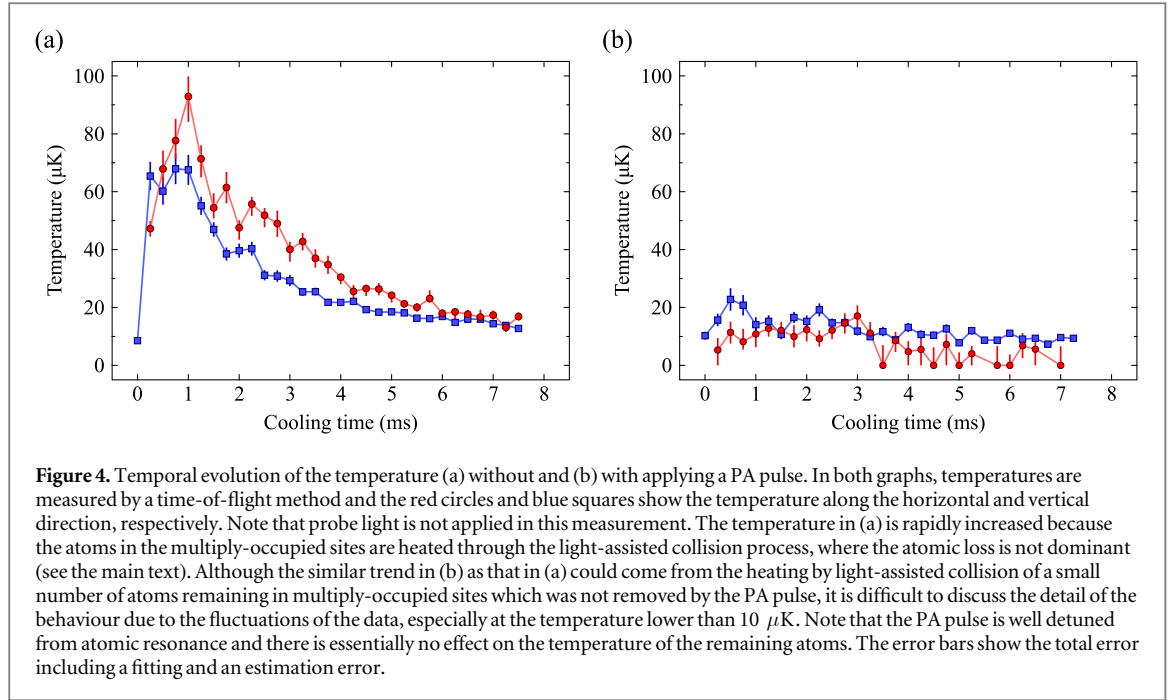
The fine tuning of the relative angle between a magnetic field and lattice laser polarizations indeed gives us a reasonably narrow resonance of the $^1S_0 - ^3P_1(m_j = 0)$ transition for atoms in the optical lattice during fluorescence imaging. Figure 3(a) shows the spectra of atoms in our deepest horizontal optical lattices of $U_x = U_y = 1500 E_R$, where $E_R = h^2/(2 m \lambda_L^2) = k_B \times 200$ nK is recoil energy of lattice beam. The top panel shows the fluorescence counts of 399 nm probe molasses light as a function of a frequency of 556 nm cooling molasses beams along the horizontal axes, in which we simultaneously apply the probe light and weak cooling molasses lights, $s_{399} \sim 1 \times 10^{-3}$ and $s_{556} \sim 0.6$, and we can observe many fluorescence counts during a 400 ms exposure time only when the cooling is efficient at favorable detunings. We obtain the optimal frequency $f_R = -337(18)$ kHz with the width of 318(12) kHz (FWHM). The bottom panel shows the optical density measured by absorption imaging with a 556 nm beam irradiated along the horizontal axis as a function of a frequency of the 556 nm probe light. In this measurement we do not apply 399 and 556 nm molasses beams. Note that we set a zero frequency detuning as the resonance frequency of this spectrum. We determine the optimal detuning of cooling beam along the horizontal axes $\delta_{556}/2\pi = f_R = -337(18)$ kHz. The same measurements are done at several horizontal lattice depths, as shown in figure 3(b). In our lattice system, Lamb-Dicke parameters are $\eta_\mu = \sqrt{\hbar k^2/(2 m \omega_\mu)} = (0.11, 0.11, 0.48)$, where k is a wavevector of 556 nm light, and $\mu = x, y, z$. Although the frequency separation between the cooling sideband f_R and the carrier transition $f = 0$, corresponding to the trap frequencies ω_x and ω_y , is not large enough compared with the natural linewidth of 184 kHz for the 556 nm cooling transition, as shown in figure 3(a), the responsible cooling mechanism along the



x - and y -axes should be sideband cooling, because the optimal detuning of cooling beam along the horizontal axis depends on the horizontal lattice trap depth and is consistent with the trap frequency along the horizontal axis, as shown in figure 3(b). We note that the shape of the resonance dose not change for all the horizontal lattice potential depths of $250 E_R$ to $1500 E_R$ studied in this measurement.

The temperature of the atoms during the fluorescence imaging is accurately measured by laser spectroscopy using the ultranarrow transition $^1S_0 - ^3P_2$ ($m_J = 0$). Figure 3(c) shows the spectrum obtained, which clearly shows three peaks corresponding to the red- and blue-sidebands and the main carrier. From the ratio of the red to the blue sideband peaks $S_R/S_B = 0.32(6)$, we can evaluate a mean oscillation quantum number in a horizontal optical lattice $\langle n \rangle = (1 - S_R/S_B)^{-1/2} - 1 = 0.22(4)$, corresponding to the atomic temperature of $k_B T_H = \hbar\omega/\ln(1 + \langle n \rangle^{-1}) = k_B \times 7.4(13) \mu\text{K}$ [46–48]. The value is in agreement with the theoretical one of $k_B T_H = \hbar\omega/\ln(1 + 16\omega^2/5\Gamma^2) = k_B \times 6.4 \mu\text{K}$ based on a sideband cooling theory [47]. Note that this expression is valid for a narrow enough laser linewidth compared to Γ and a low enough laser power that there is no need to consider a saturation effect. The temperature along the vertical direction is measured by a time-of-flight method to be $12(1) \mu\text{K}$. The optimal detunings are determined for various lattice depths, and are independent of the lattice depth, which suggests that the dominant cooling mechanism is Doppler cooling. This is reasonable if we consider the small trap frequency of 15.7 kHz along the vertical direction compared with the linewidth of 184 kHz.

The unique feature of our scheme is the separation of the cooling and probing processes during the fluorescence imaging. We can therefore study the effect of the cooling beams alone. Here we study the temporal evolution of the temperature with narrow-line laser cooling, especially at the early stage of cooling, to investigate what happens during the cooling process. This is especially interesting because the atom loss rate for the light-assisted collision associated with the $^1S_0 + ^3P_1$ states is small [49] and the atoms in multiply-occupied sites would be heated without loss, differently from the case of alkali atoms. In this measurement, the temperature is measured by a time-of-flight method with absorption imaging. To correctly estimate the temperature along the horizontal axis, we numerically calculate the size of the atom cloud after a time-of-flight, assuming an initial



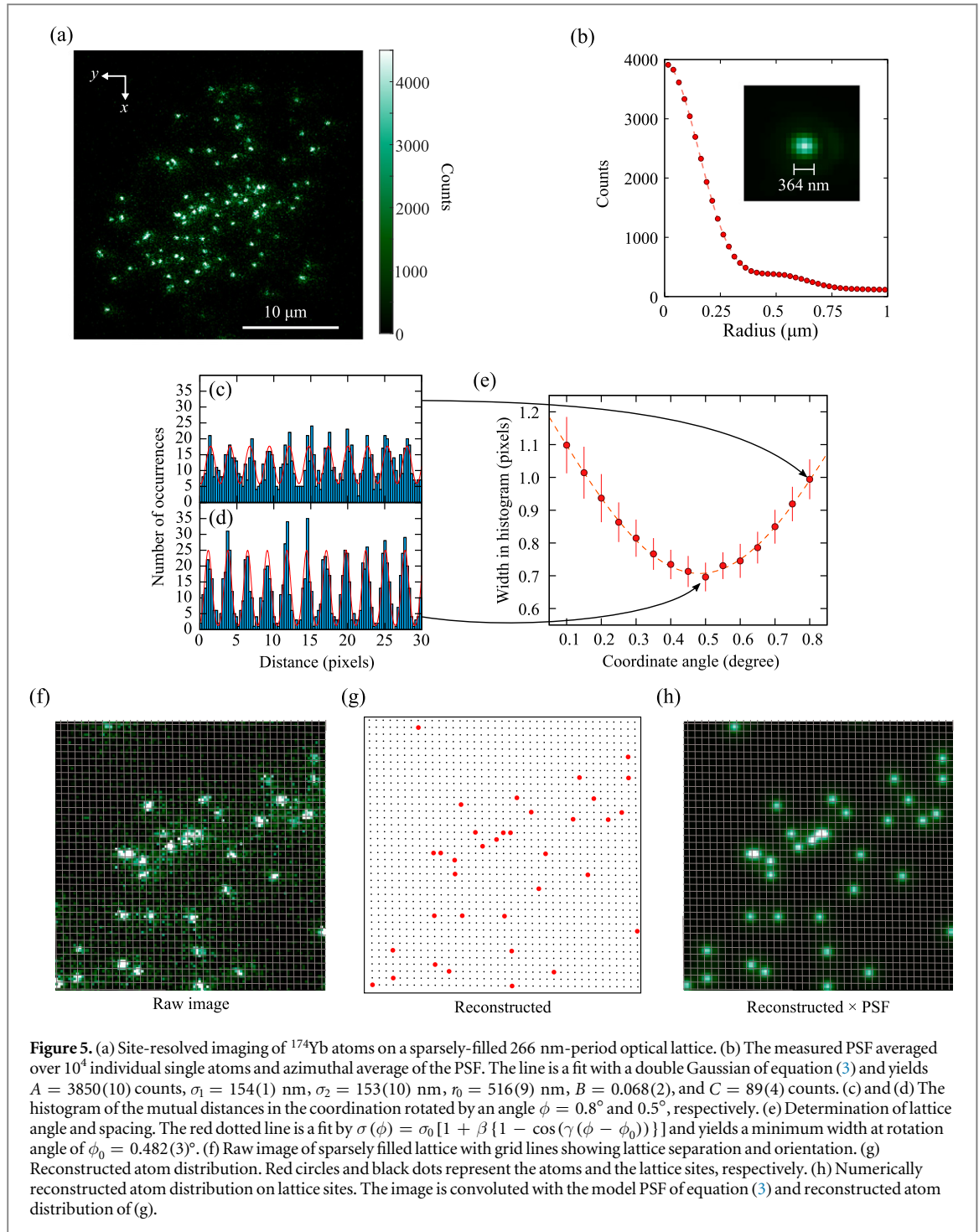
Boltzman occupation of the each vibrational level and a ballistic expansion of the cloud. Figure 4(a) shows the results of the measurements. The temperatures rapidly increase within several milliseconds followed by the rather slow decrease towards the steady-state value obtained by the ultranarrow line laser spectroscopy of figure 3(c). This behaviour is explained as an effect of a light-assisted collision due to the near-resonant cooling light. Namely, atoms in multiply-occupied sites should be heated by release of the kinetic energy subsequent on a light-assisted collision. This is confirmed by further measurements with applying a photoassociation (PA) pulse for removal of multiply-occupied sites before imaging, shown in figure 4(b). In spite of the fluctuation of data, it is clear that the behaviour of the temperatures of figure 4(b) is different from that of figure 4(a). Although all the following single-site resolved imaging data presented in this paper are measured without the application of PA light, this initial heating effect is negligible because the multiply-occupied sites are almost absent in sparse atomic samples used for our QGM measurement.

4. Site-resolved imaging

We image the atomic fluorescence onto the EMCCD camera (Andor iXon^{EM} Blue). In figure 5(a) we show one illustrative example of the obtained images. Note that, just before the fluorescence imaging, we intentionally select only about 2% of the atoms for easier evaluation of the performance of the QGM. Such dilution of the atoms is done by performing a weak excitation with the $^1\text{S}_0\text{-}^3\text{P}_2(m_f = -1)$ transition, and then returning the atoms back into the ground state $^1\text{S}_0$. Figure 5(b) shows our measured point spread function (PSF), obtained by averaging over 10^4 fluorescence images of individual atoms. We find that our PSF can be well approximated by a double Gaussian:

$$\text{PSF}(r) = A \left[\exp\left(-\frac{r^2}{2\sigma_1^2}\right) + B \exp\left(-\frac{1}{2}\left(\frac{r-r_0}{\sigma_2}\right)^2\right) \right] + C \quad (3)$$

with widths σ_1 , σ_2 , main and relative amplitudes A , B , a spatial offset r_0 , and an overall count offset C . The fit result shows our PSF is well described with $\sigma_1 = 154(1)$ nm and $\sigma_2 = 153(10)$ nm, and also has a FWHM of 364 nm, and we detect on average 200 photons per atom within 400 ms fluorescence time. In our imaging system, the spherical aberration remains, making the resolution of PSF worse than ideal one. Our system has a total fluorescence collection efficiency of 6.0%, given by the objective's solid angle of $\Omega/4\pi = 17\%$, 51% total transmission through the imaging optics, and quantum efficiency of 70% of our EMCCD camera. The corresponding atomic fluorescence rate of ~ 8300 photons/s is large enough to unambiguously identify the presence or absence of an atom for each lattice site. Note that the maximum number of detected photons is limited by the cooling rate of the narrow transition [44]. Although the resolution of measured PSF is about 1.4 times larger than the lattice spacing, we successfully determine the atomic distribution by deconvolution of images.



For reconstructing an atom distribution from our obtained images, we first determine a lattice angle and spacing from the isolated, single-site resolved signals [8]. Our lattice axes are oriented approximately along the vertical and horizontal axes with respect to the images. The histogram of the mutual distances in the coordination rotated by a small angle ϕ is shown in figure 5(c) and (d). We fit a periodic array of Gaussians to the observed histogram. Figure 5(e) shows the width of the Gaussians in the histogram as a function of a coordinate rotation angle. The red dotted line is a fit by $\sigma(\phi) = \sigma_0 [1 + \beta \{1 - \cos(\gamma(\phi - \phi_0))\}]$. The minimum width of the histogram is obtained at the coordinate rotation angle of $0.482(3)^\circ$ and the lattice constant of 2.66(1) pixels on CCD plane corresponding to the lattice constant of 266 nm. From the same analysis of the other lattice axis, we also obtain the coordinate rotation angle of $-0.664(4)^\circ$ and lattice constant of 2.65(1) pixels on CCD plane corresponding to the lattice constant of 266 nm. Thus, the magnification ratio of our imaging system is 159.7(4) and one pixel of our CCD camera corresponds to 100.2(3) nm on the objective plane. These values are used for the deconvolution analysis of our images. Figure 5(f) shows a raw image of the limited region of

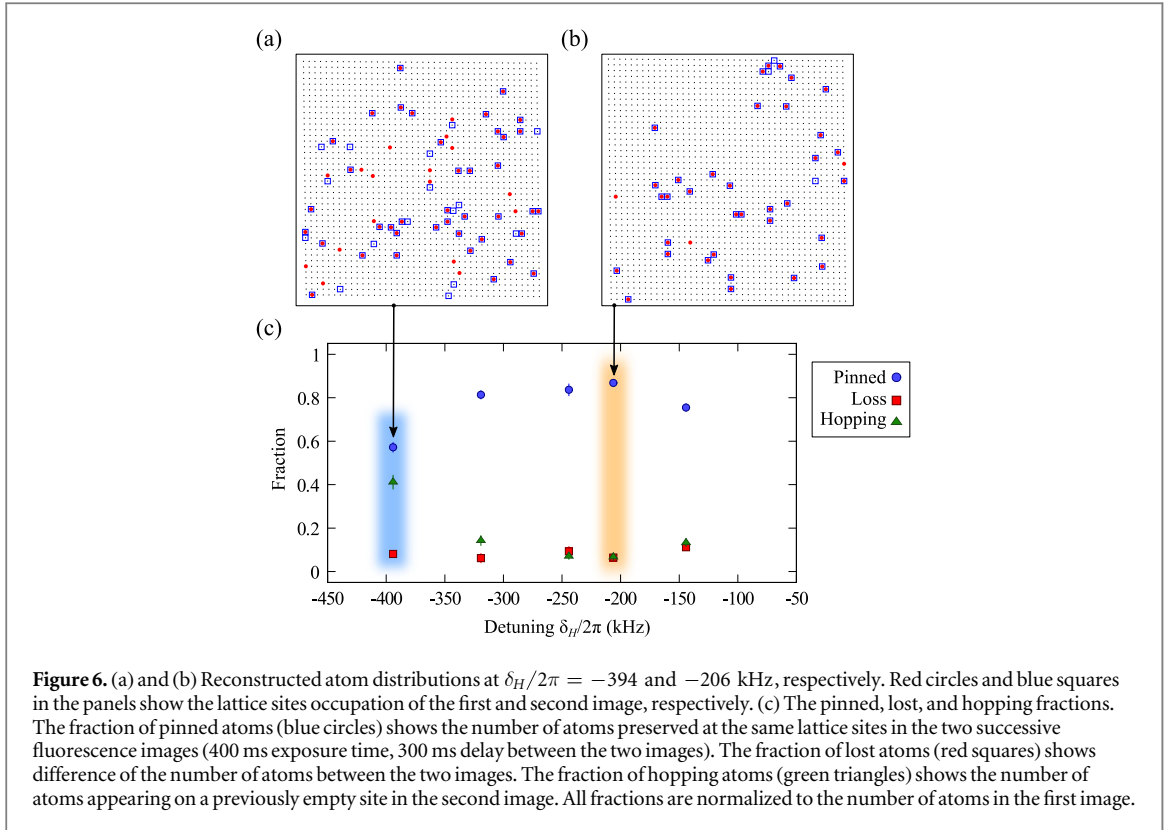
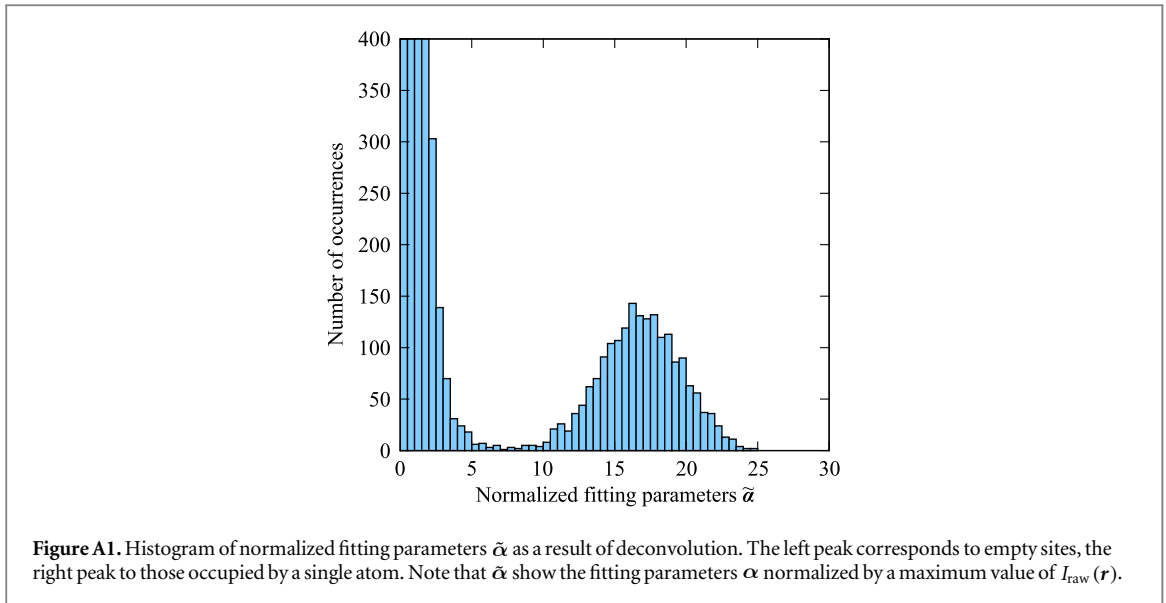


figure 5(a) with grid lines showing lattice separation and orientation. In figure 5(g), we show a reconstructed atom distribution where red circles and black dots represent the atoms and the lattice sites, respectively. In figure 5(h), we also show the reconstructed atom distribution convoluted with the model PSF of equation (3), which is compared with the raw image of figure 5(f).

An important aspect of QGM is the high-fidelity of the imaging process characterized by loss and hopping rates during the fluorescence imaging. For this purpose, we take two successive images of the same atoms with 400 ms exposure time and 300 ms delay between the two images, and observe the change in the distribution. We precisely tune the detuning δ_H of cooling molasses along the horizontal axes, and evaluate the loss and hopping rates during the fluorescence image from the two successive images. Figure 6(a) and (b) show the results of reconstructed atom distributions at $\delta_H/2\pi = -394$ and -206 kHz, respectively. For optimized parameters, we achieve loss rates of 6.5(18)% and hopping rates of 6.7(15)% for 400 ms exposures of clouds with fillings of ~ 0.02 (see figure 6(c)). These rates, which include reconstruction errors, give a detection fidelity of 87(2)% for sparse clouds. Here we discuss the origins of the measured loss and hopping rates. The thermal hopping cannot explain the observed rates since the average occupation number during the fluorescence imaging is as low as 0.22. Instead, several possible mechanisms can be considered such as the branching from the 1P_1 to lower states [50], a vibrational quantum number-changing transition during the absorption and fluorescence cycle of the 1S_0 - 1P_1 transition, and the photon scattering from the 3P_1 state due to the 532 nm lattice beams. The loss rate estimated with the lifetime about 10 s during fluorescence imaging is 6.8%. This value is in good agreement with the measured loss rate. We also note that one of the limiting factors of the lifetime is the irradiation of the 399 nm probe light itself.

5. Conclusion

In conclusion, we demonstrate a bosonic ^{174}Yb QGM for a 2D optical lattice with a short lattice constant of 266 nm. The atoms are preserved in the lattice sites during fluorescence imaging by narrow-line laser cooling which successfully combines Doppler cooling and sideband cooling. The resulting temperature is $T = 7.4(13)$ μK , corresponding to a mean oscillation quantum number along the horizontal axes 0.22(4). The PSF has a reasonably small width comparable to the ideal value, enabling the identification of the presence and absence of atoms by the deconvolution analysis. The high fidelity of the imaging process, which is an important aspect of QGM, is confirmed by the measurement of loss rate of 6.5(18)% and hopping rate of 6.7(15)% for 400 ms exposure time.



While we perform the experiment with bosonic ^{174}Yb atoms, our method is applicable for a QGM for other Yb isotopes, including fermionic ^{171}Yb and ^{173}Yb . In fact, our preliminary result shows that we can successfully obtain site-resolved images for fermionic ^{171}Yb atoms. In addition, the sideband cooling demonstrated in this work can be straightforwardly applied to other alkaline-earth atoms such as strontium, especially for an optical lattice with magic wavelength. The realization of a QGM with enough fidelity for Yb atoms in a Hubbard-regime optical lattice opens up the possibilities for studying various kinds of quantum many-body systems, and also long-range-interacting systems such as Rydberg states.

Acknowledgments

We would like to thank K Shibata for the setup of this experiment and T Fukuhara for useful discussions. This work was supported by the Grant-in-Aid for Scientific Research of JSPS (Nos. 13J00122, 25220711, 26247064, 26610121) and the Impulsing Paradigm Change through Disruptive Technologies (ImpACT) program.

Appendix. Deconvolution procedure

Here we describe the deconvolution procedure of our fluorescence image. First step is to determine a PSF, a lattice spacing, and a coordinate rotation angle from the isolated, single-site resolved signals, as is explained in detail in section 4. From the determined PSF of equation (3) and the location of lattice sites, we next calculate a trial image

$$I_{\text{est}}(\mathbf{r}, \boldsymbol{\alpha}) = \sum_n \alpha_n \text{PSF}(|\mathbf{r} - \mathbf{r}_n|), \quad (\text{A.1})$$

where \mathbf{r} represents a position in an image plane, \mathbf{r}_n a position of a lattice site n , α_n a fitting parameter corresponding to a probability of finding an atom at a lattice site n , and $\boldsymbol{\alpha} = (\alpha_1, \alpha_2, \alpha_3, \dots, \alpha_n)$. Note that α_n represents a fitted value of a peak fluorescence count at the n -th lattice site. Finally we determine the parameters $\boldsymbol{\alpha}$ by minimizing a quantity $\Delta(\boldsymbol{\alpha}) = \sum_{\mathbf{r}} (I_{\text{raw}}(\mathbf{r}) - I_{\text{est}}(\mathbf{r}, \boldsymbol{\alpha}))^2$, where $I_{\text{raw}}(\mathbf{r})$ is a raw fluorescence image. As a typical example of this deconvolution procedure, we show in figure A1 a histogram of α_n determined in several regions of 9×9 sites picked up from raw images.

References

- [1] Jaksch D and Zoller P 2005 *Annals Phys.* **315** 52–79
- [2] Greiner M, Mandel O, Esslinger T, Hänsch T W and Bloch I 2002 *Nature* **415** 39–44
- [3] Stöferle T, Moritz H, Schori C, Köhl M and Esslinger T 2004 *Phys. Rev. Lett.* **92** 130403
- [4] Spielman I B, Phillips W D and Porto J V 2007 *Phys. Rev. Lett.* **98** 080404
- [5] Schneider U, Hackermüller L, Will S, Best T, Bloch I, Costi T A, Helmes R W, Rasch D and Rosch A 2008 *Science* **322** 1520–5
- [6] Jördens R, Strohmaier N, Günter K, Moritz H and Esslinger T 2008 *Nature* **445** 204–7
- [7] Bakr W S, Gillen J I, Peng A, Fölling S and Greiner M 2009 *Nature* **462** 74–7
- [8] Sherson J F, Weitenberg C, Endres M, Cheneau M, Bloch I and Kuhr S 2010 *Nature* **467** 68–72

- [9] Bakr W S, Peng A, Tai M E, Ma R, Simon J, Gillen J I, Foelling S, Pollet L and Greiner M 2010 *Science* **329** 547–50
- [10] Preiss P M, Ma R, Tai M E, Lukin A, Rispoli M, Zupancic P, Lahini Y, Islam R and Greiner M 2015 *Science* **347** 1229–33
- [11] Fukuhara T *et al* 2013 *Nat. Phys.* **9** 235–41
- [12] Cheneau M, Barmettler P, Poletti D, Endres M, Schauß P, Fukuhara T, Gross C, Bloch I, Kollath C and Kuhr S 2012 *Nature* **481** 484–7
- [13] Cheuk L W, Nichols M A, Okan M, Gersdorf T, Ramasesh V V, Bakr W S, Lompe T and Zwierlein M W 2015 *Phys. Rev. Lett.* **114** 193001
- [14] Haller E, Hudson J, Kelly A, Cotta D A, Peucedercf B, Bruce G D and Kuhr S 2015 *Nat. Phys.* **11** 738–42
- [15] Edge G J A, Anderson R, Jervis D, McKay D C, Day R, Trotzky S and Thywissen J H 2015 *Phys. Rev. A* **92** 063406
- [16] Parsons M F, Huber F, Mazurenko A, Chiu C S, Setiawan W, Wooley-Brown K, Blatt S and Greiner M 2015 *Phys. Rev. Lett.* **114** 213002
- [17] Omran A, Boll M, Hilker T, Kleinlein K, Salomon G, Bloch I and Gross C 2015 arXiv:1510.04599
- [18] Greif D, Parsons M F, Mazurenko A, Chiu C S, Blatt S, Huber F, Ji G and Greiner M 2015 arXiv:1511.06366
- [19] Cazalilla M, Ho A and Ueda M 2009 *New J. Phys.* **11** 103033
- [20] Taie S, Yamazaki R, Sugawa S and Takahashi Y 2012 *Nat. Phys.* **8** 825–30
- [21] Hazzard K R A, Gurarie V, Hermele M and Rey A M 2012 *Phys. Rev. A* **85** 041604
- [22] Pagano G *et al* 2014 *Nat. Phys.* **10** 198–201
- [23] Gorshkov A, Hermele M, Gurarie V, Xu C, Julienne P, Ye J, Zoller P, Demler E, Lukin M and Rey A 2010 *Nat. Phys.* **6** 289–95
- [24] Scazza F, Hööfrichter C, Hfer M, De Groot P, Bloch I and Fölling S 2014 *Nat. Phys.* **10** 779–84
- [25] Zhang X, Bishof M, Bromley S, Kraus C, Safronova M, Zoller P, Rey A and Ye J 2014 *Science* **345** 1467–73
- [26] Cappellini G *et al* 2014 *Phys. Rev. Lett.* **113** 120402
- [27] Mancini M *et al* 2015 *Science* **349** 1510–3
- [28] Sugawa S, Yamazaki R, Taie S and Takahashi Y 2011 *Phys. Rev. A* **84** 011610
- [29] Stellmer S, Grimm R and Schreck F 2013 *Phys. Rev. A* **87** 013611
- [30] Tey M K, Stellmer S, Grimm R and Schreck F 2010 *Phys. Rev. A* **82** 011608
- [31] Sugawa S, Inaba K, Taie S, Yamazaki R, Yamashita M and Takahashi Y 2011 *Nat. Phys.* **7** 642–8
- [32] Derevianko A and Cannon C C 2004 *Phys. Rev. A* **70** 062319
- [33] Daley A J, Boyd M M, Ye J and Zoller P 2008 *Phys. Rev. Lett.* **101** 170504
- [34] Gorshkov A V, Rey A M, Daley A J, Boyd M M, Ye J, Zoller P and Lukin M D 2009 *Phys. Rev. Lett.* **102** 110503
- [35] Shibata K, Kato S, Yamaguchi A, Uetake S and Takahashi Y 2009 *Appl. Phys. B* **97** 753–8
- [36] Kato S, Sugawa S, Shibata K, Yamamoto R and Takahashi Y 2013 *Phys. Rev. Lett.* **110** 173201
- [37] Yamaguchi A, Uetake S, Kato S, Ito H and Takahashi Y 2010 *New J. Phys.* **12** 103001
- [38] Millen J, Lochead G and Jones M P A 2010 *Phys. Rev. Lett.* **105** 213004
- [39] McQuillen P, Zhang X, Strickler T, Dunning F B and Killian T C 2013 *Phys. Rev. A* **87** 013407
- [40] Mukherjee R, Millen J, Nath R, Jones M and Pohl T 2011 *J. Phys. B: At. Mol. Opt. Phys.* **44** 184010
- [41] Miranda M, Inoue R, Okuyama Y, Nakamoto A and Kozuma M 2015 *Phys. Rev. A* **91** 063414
- [42] Fukuhara T, Sugawa S, Sugimoto M, Taie S and Takahashi Y 2009 *Phys. Rev. A* **79** 041604
- [43] Kato S, Shibata K, Yamamoto R, Yoshikawa Y and Takahashi Y 2012 *Appl. Phys. B* **108** 31–8
- [44] Shibata K, Yamamoto R and Takahashi Y 2014 *J. Phys. Soc. Jpn.* **83** 014301
- [45] Le Kien F, Schneeweiss P and Rauschenbeutel A 2013 *Eur. Phys. J. D* **67** 92
- [46] Wineland D J and Itano W M 1979 *Phys. Rev. A* **20** 1521–40
- [47] Wineland D J, Itano W M, Bergquist J C and Hulet R G 1987 *Phys. Rev. A* **36** 2220–32
- [48] Diedrich F, Bergquist J C, Itano W M and Wineland D J 1989 *Phys. Rev. Lett.* **62** 403–6
- [49] Lee J, Lee J H, Noh J and Mun J 2015 *Phys. Rev. A* **91** 053405
- [50] Honda K, Takahashi Y, Kuwamoto T, Fujimoto M, Toyoda K, Ishikawa K and Yabuzaki T 1999 *Phys. Rev. A* **59** R934–7